







High-pressure annealing driven nanocrystal formation in $Zr_{50}Cu_{40}Al_{10}$ metallic glass and strength increase

Yuki Shibazaki^{1,9}, Rui Yamada², Junji Saida², Yoshio Kono^{3,4}, Masato Wakeda⁵, Keiji Itoh⁶, Masahiko Nishijima⁷ & Koji Kimoto⁸

Pressure-induced structural changes in metallic glasses have been of great interest as they are expected to open new ways to synthesize novel materials with unexpected properties. Here, we investigated the effect of simultaneous high-pressure and high-temperature treatment on the structure and properties of a $Zr_{50}Cu_{40}Al_{10}$ metallic glass by in situ X-ray structure measurement and property analysis of the final material. We found the unusual formation of Cu-rich nanocrystals at high pressure and temperature, accompanied by significant strength and hardness enhancement. Based on reverse Monte Carlo modeling and molecular dynamics simulations, the structure of the metallic glass changed to a densely packed, chemically uniform configuration with high short-range and medium-range ordering at high pressure and temperature. These results show that high-pressure annealing processes provide a new way to improve and control properties without changing their composition.

¹International Center for Young Scientists, National Institute for Materials Science, 1-1 Namiki, Tsukuba 305-0044, Japan. ²Frontier Research Institute for Interdisciplinary Sciences, Tohoku University, 6-3 Aoba, Aramaki, Aoba-ku, Sendai 980-8578, Japan. ³Geophysical Laboratory, Carnegie Institution of Washington, 9700S. Cass Ave., Argonne, IL 60439, USA. ⁴Geodynamics Research Center, Ehime University, 2-5 Bunkyo-cho, Matsuyama 790-8577, Japan. ⁵Research Center for Structural Materials, National Institute for Materials Science, 1-2-1 Sengen, Tsukuba 305-0047, Japan. ⁶Graduate School of Education, Okayama University, 3-1-1 Tsushima-Naka, Kita-ku, Okayama 700-8530, Japan. ⁷The Electron Microscopy Center, Tohoku University, 2-1-1 Katahira, Aoba-ku, Sendai 980-8577, Japan. ⁸Electron Microscopy Group, Research Center for Advanced Measurement and Characterization, National Institute for Materials Science, 1-1 Namiki, Tsukuba 305-0044, Japan. ⁹Present address: Institute of Materials Structure Science, High Energy Accelerator Research Organization (KEK), 1-1 Oho, Tsukuba 305-0801, Japan. ✉email: yuki.shibazaki@kek.jp

Metals glasses (MGs), including “bulk MGs (BMGs)”, have attracted considerable interest in the field of materials science for scientific research and industrial requirements because of their excellent properties, such as high corrosion resistance¹, high strength², large elastic elongation³, and good magnetic softness⁴. High pressure has received attention as a useful tool to modify the random atomic configuration of BMGs, which influences on the glass transition (T_g), crystallization (T_x) temperatures^{5–7}, and physical properties⁸.

The discovery of pressure-induced structural changes in MGs attracted the great interest of scientists in the field of condensed matter physics as a peculiar phenomenon. An excellent example of a structural change in MGs is a pressure-induced amorphous-to-amorphous transition, i.e., polyamorphism. The pressure-induced polyamorphism was first reported in a $\text{Ce}_{55}\text{Al}_{45}$ MG by Sheng et al.⁹, using the synchrotron X-ray diffraction technique. Subsequently, similar polyamorphic transitions have been observed in other lanthanide-based MGs^{10–13}. This transition has been explained by the delocalization of $4f$ electrons in lanthanide elements^{9,11}. However, the polyamorphic transition of the lanthanide-based MGs induced by room-temperature compression is a reversible process⁹ and the high-pressure structure formed after the polyamorphic transition is unquenchable to the ambient-pressure condition.

Dmowski et al.¹⁴ proposed that liquid-to-liquid transition occurs in Zr-based MGs, when they are heated to the supercooled liquid state under high-pressure conditions ($\sim 4\text{--}8$ GPa). Notably, the high-pressure structure reported in Dmowski et al.¹⁴ is quenchable to room-pressure condition. The discovery of the quenchable high-pressure and high-temperature amorphous structure in Zr-based MGs is expected to open a new way to synthesize new MG materials, with unexpected structural and physical properties. However, the previous study¹⁴ focused only on the nature of the liquid-to-liquid transition and did not investigate the influence of structural change from the viewpoint of quenchable materials properties. Molecular dynamics (MD) simulations predicted that high-pressure annealing of the $\text{Zr}_{50}\text{Cu}_{40}\text{Al}_{10}$ MG causes better plastic performance compared to the as-cast state, and larger strength and stiffness compared to the glass treated by conventional ambient-pressure annealing¹⁵. In fact, we confirmed that the quenchable high-pressure and high-temperature structure in $\text{Zr}_{50}\text{Cu}_{40}\text{Al}_{10}$ BMG proposed by Dmowski et al.¹⁴ has improved strength and ductility with the ultra-high density¹⁶. Therefore, previous high-pressure and high-temperature studies suggest that high-pressure annealing provides potential for producing a new type of BMGs with exceptional mechanical properties, which cannot otherwise be achieved by conventional synthesis methods at an ambient pressure. However, because the pressure and temperature conditions of previous studies^{14,16} were limited, the effects of high-pressure annealing, particularly the behavior of BMGs at higher temperatures, mechanical properties, and crystallization process, as well as structures, are still not clearly understood.

In this study, we utilize in situ synchrotron X-ray diffraction by combined it with reverse Monte Carlo (RMC) modeling, a MD simulation, and transmission electron microscope observations and analyze the mechanical properties of $\text{Zr}_{50}\text{Cu}_{40}\text{Al}_{10}$ BMG treated at high pressure and temperature, in order to investigate the effect of high-pressure annealing on the structure and properties of the BMG. We found the unusual formation of densely distributed Cu-rich nanocrystallized $\text{Zr}_{50}\text{Cu}_{40}\text{Al}_{10}$ BMG above the temperature of the structural change at a high pressure of 5.5 GPa. The RMC modeling and MD simulation showed that the high-pressure and high-temperature treatment increases the number of Zr–Cu pairs in $\text{Zr}_{50}\text{Cu}_{40}\text{Al}_{10}$ BMG, resulting in structural changes to a relatively chemical-uniform configuration

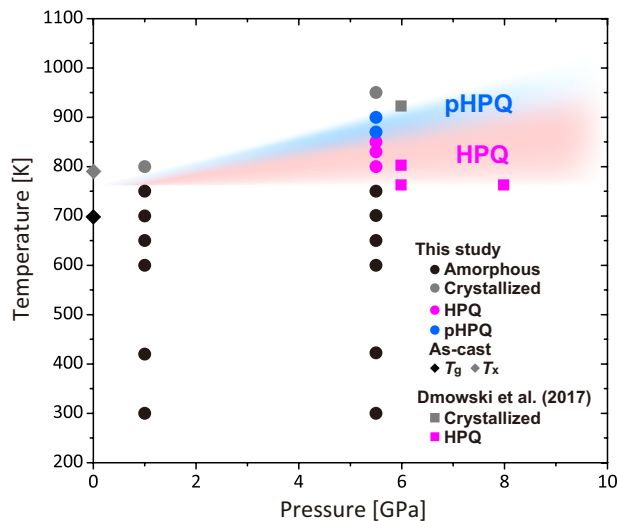


Fig. 1 Experimental pressure and temperature conditions and the sample states identified by synchrotron X-ray diffraction technique. Black and gray symbols denote the amorphous and crystallized samples, respectively. Purple and blue circles denote the high-pressure quenched (HPQ) and post HPQ (pHPQ) states, respectively (see text). Black and gray diamonds denote the glass transition (T_g) and crystallization temperatures (T_x) of the as-cast $\text{Zr}_{50}\text{Cu}_{40}\text{Al}_{10}$ BMG, measured by a differential scanning calorimetry. Purple and gray squares denote the pressure and temperature conditions where the HPQ and crystallized samples of the $\text{Zr}_{50}\text{Cu}_{40}\text{Al}_{10}$ BMG were reported by Dmowski et al.¹⁴. Red and blue shaded areas indicate the expected ranges of the HPQ and pHPQ states in the $\text{Zr}_{50}\text{Cu}_{40}\text{Al}_{10}$ BMG, respectively.

with high short-range and medium-range orderings. The Cu-rich nanocrystal may be nucleated based on the orderings formed by the structural change at high pressure and high temperature. The nanocrystallization significantly improved the hardness and strength of the $\text{Zr}_{50}\text{Cu}_{40}\text{Al}_{10}$ BMG, which cannot be achieved by conventional ambient-pressure nanocrystallization process. High-pressure and high-temperature annealing process provides a great potential for creating unusual textures in MGs, leading to new procedures for the improvement and control of properties without changing the composition.

Results

In situ structure measurement at high pressures. Figure 1 shows the experimental pressure and temperature conditions, and the states of the $\text{Zr}_{50}\text{Cu}_{40}\text{Al}_{10}$ BMG sample. This was investigated via in situ structure measurement under high-pressure conditions using multi-angle energy dispersive X-ray diffraction (EDXD) technique at the beamline 16-BM-B in the Advanced Photon Source, USA. At 1.0 GPa (Run-1), the structure factors, $S(Q)$, of the $\text{Zr}_{50}\text{Cu}_{40}\text{Al}_{10}$ BMG show the typical amorphous feature with no notable change until the crystallization temperature of 800 K (Fig. 2a). On the contrary, we observe a considerable change in $S(Q)$ at 5.5 GPa (Run-2). The $S(Q)$ up to 850 K is comparable to that of the as-cast glass (Fig. 2b), whereas the broad peaks of $S(Q)$ become significantly sharper and clear at 900 K, with the appearance of oscillations $>7 \text{ \AA}^{-1}$ (Fig. 2b). The sharpening of the broad peaks of $S(Q)$ is generally linked to the ordering of the disordered amorphous structure. Sharp peaks from crystals are observed by further heating the sample to 950 K. To confirm the repeatability of the change in $S(Q)$ and possible quench ability of the sample after the change at 900 K, we conducted an additional experiment at 5.5 GPa up to 870 K (Run-3). Similar to Run-2, we do not observe any major changes in $S(Q)$ up to 850 K and the

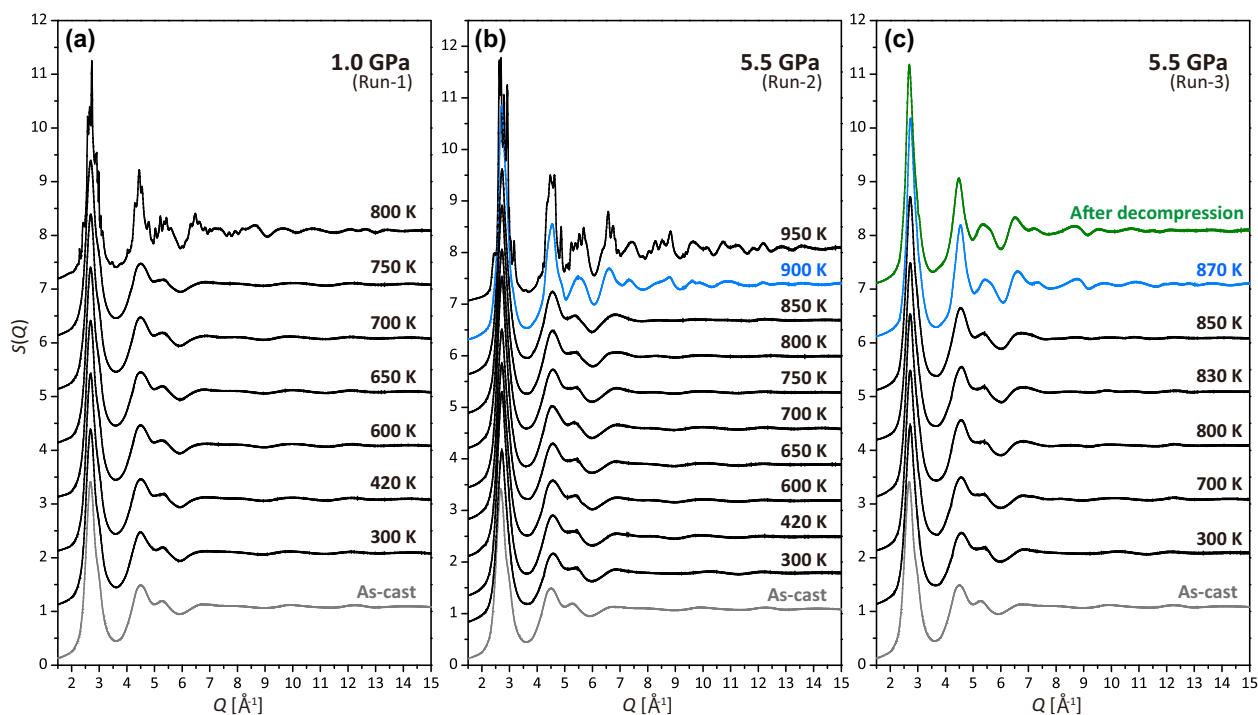


Fig. 2 Structure factors $S(Q)$ of $Zr_{50}Cu_{40}Al_{10}$ BMG at high pressures. **a** $S(Q)$ at 1.0 GPa (Run-1). **b** $S(Q)$ at 5.5 GPa up to the temperature where sharp peaks from crystal were observed (Run-2). **c** $S(Q)$ at 5.5 GPa below the temperature where sharp crystal peaks were observed in Run-2 and after decompression (Run-3). Temperature values indicate synthesized temperature conditions. The data are shifted by 1.0 in **a** and **c**, and 0.7 in **b** for clarity.

marked change in $S(Q)$ appears again at 870 K and 5.5 GPa (Fig. 2c). We found that the $S(Q)$ at 870 K and 5.5 GPa remains at ambient-pressure and room-temperature condition (uppermost $S(Q)$ in Fig. 2c), indicating that it is quenchable.

Figure 3 shows the pair distribution functions, $g(r)$, obtained by the Fourier transform of the $S(Q)$ shown in Fig. 2c. The as-cast glass exhibits the double-peak feature of the first peak in $g(r)$. Based on a previous study¹⁷, the two first peaks (~ 2.8 Å and ~ 3.1 Å) correspond to the first neighbor distances of Zr–Cu and Zr–Zr atomic pairs, respectively. The double-peak feature remains at low-temperature conditions <700 K at 5.5 GPa, whereas it changes to the single-peak feature at 800 K and 5.5 GPa (Fig. 3). We also observe similar $g(r)$ at 830 and 850 K at 5.5 GPa (Fig. 3). The change of the first peak of $g(r)$ from the double-peak feature to the single-peak feature, and the pressure and temperature conditions of the change are consistent with those of the liquid-to-liquid phase transition proposed by the previous study¹⁴ (Fig. 1). Hereafter, we denote the glass between 800 and 850 K at 5.5 GPa as a high-pressure quenched (HPQ) glass, as per the previous study¹⁴.

In addition, we found that $g(r)$ changes considerably by further heating to 870 K. The first (~ 3 Å), second (~ 5 Å), and third (~ 7.5 Å) broad peaks become significantly sharper, accompanied by an increase in those intensities, and the small subpeaks at ~ 6 Å and ~ 9 Å become distinct (Fig. 3). The feature of $g(r)$ is preserved even after depressurization and cooling to ambient-pressure and room-temperature condition (uppermost $g(r)$ in Fig. 3).

To the best of our knowledge, the $S(Q)$ observed at 5.5 GPa and 870 and 900 K (Fig. 2b, c), with the high-intensity relatively sharp peaks without sharp Bragg's peaks from the crystals, has not been reported by previous ambient-pressure studies. We also did not observe such unique $S(Q)$ and $g(r)$ patterns at 1.0 GPa, regardless of the same heating step as the experiments at 5.5 GPa (50 K steps; Fig. 2a). Therefore, the high pressure of 5.5 GPa enables us to observe the $Zr_{50}Cu_{40}Al_{10}$ sample showing the unique $S(Q)$ and

$g(r)$ patterns that are hardly obtainable at ambient and low pressures, such as 1.0 GPa. We denote the glass between 870 and 900 K at 5.5 GPa as the post HPQ (pHPQ) glass.

Microstructure observations by scanning transmission electron microscope. We investigated the cross section of the samples using a scanning transmission electron microscope (STEM) to understand the origin of the $S(Q)$ and $g(r)$ of the pHPQ sample. The low-magnification bright-field (BF)-STEM image shows no contrast, indicating no typical ordering at the 100-nm scale in the pHPQ sample (Fig. 4). In contrast, the high-magnification BF-STEM image of the sample reveals the existence of a nanometer-scale ordering and a disordered random region in the pHPQ sample (Fig. 5a). The typical size of the nano-ordered region is <5 nm. We estimated the typical intervals in the nano-ordered region and obtained the first, second, and third-neighbor distances of ~ 3.0 Å, ~ 5.0 Å, and ~ 7.6 Å, respectively (Fig. 5b). Interestingly, the neighbor distances are consistent with the enhanced peak positions of $g(r)$ after the change to the pHPQ sample (Fig. 5c). Therefore, we consider that the change to the pHPQ sample at 5.5 GPa and 870 K is caused by the nanometer-scale ordering.

In addition, the annular dark-field (ADF)-STEM image (Fig. 6a) shows a compositional inhomogeneity in the pHPQ sample at the nanometer scale. Energy dispersive X-ray spectroscopy (EDS) mapping analyses reveal that Zr and Cu have compositional fluctuations (Fig. 7). The bright region in the ADF-STEM image has a Zr-poor and Cu-rich composition, while the dark region has a Zr-rich and Cu-poor composition (Fig. 7). Even though it is difficult to accurately perform a quantitative analysis due to the small scale of the bright and dark regions (<10 nm), the bright region in the ADF-STEM image consists of ~ 33 at.% Zr, 59 at.% Cu, and 8 at.% Al.

The high-magnification STEM images (Fig. 6b) also show lattice-fringe-like contrast in the Cu-rich area (the bright region

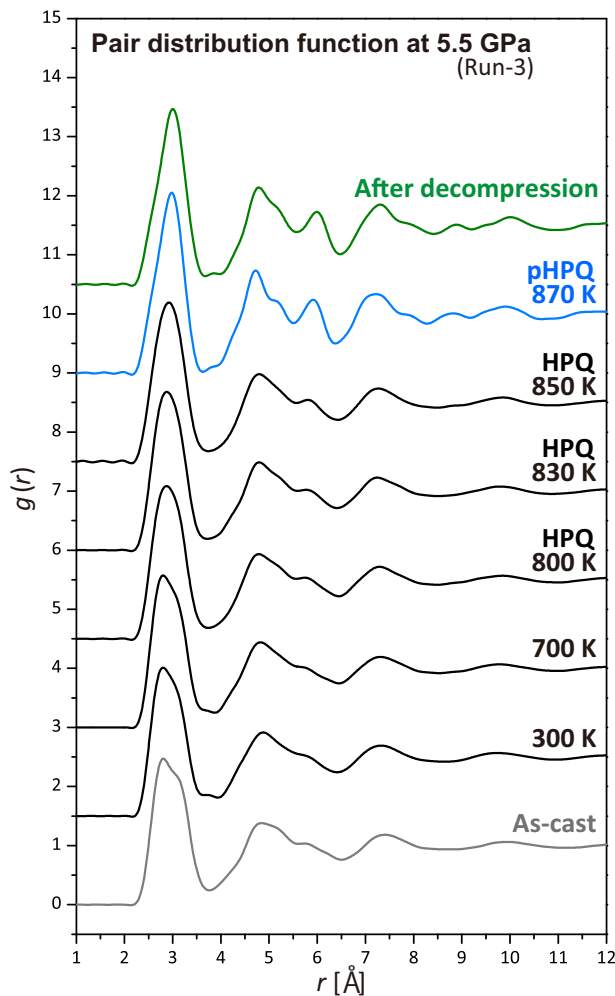


Fig. 3 Pair distribution functions $g(r)$ of $\text{Zr}_{50}\text{Cu}_{40}\text{Al}_{10}$ BMG at 5.5 GPa. $g(r)$ obtained from $S(Q)$ at 5.5 GPa and after decompression (Run-3). Temperature values indicate synthesized temperature conditions. The data are shifted by 1.5 for clarity.

in the ADF-STEM image and the dark region in the annular BF (ABF)-STEM image), corresponding to the nano-ordered region in Fig. 5. In addition, the Cu-rich area (e.g., the dotted square region in Fig. 6b) appears to consist of a few ordered domains with different directions. This indicates that the size of each ordered domain is only a few nanometers. The mapping experiment of nanobeam electron diffraction with a probe size of 2 nm (full-width at half-maximum) shows weak, but clear diffraction spots in the Cu-rich area (Fig. 6c). On the contrary, the Zr-rich area (the dark region in the ADF-STEM image and the bright region in the ABF-STEM image) does not exhibit the clear lattice-fringe-like contrast (Fig. 6b), and we do not observe the diffraction spots in this area. Therefore, we considered that the Cu-rich area is nanocrystallized in the pHPQ sample, while the Zr-rich area has the amorphous structure.

The ADF-STEM image shows another remarkable texture of the pHPQ sample. The Cu-rich bright region is densely distributed and appears to form a network. This means that the nanometer-size residual Zr-rich amorphous regions are isolated and surrounded by the Cu-rich nanocrystallized walls (Fig. 6). The volume fraction of the Cu-rich area, i.e., the Cu-rich nanocrystal, is broadly estimated to be 60–70% from the ADF-STEM image (Fig. 6a). The STEM observations show that the

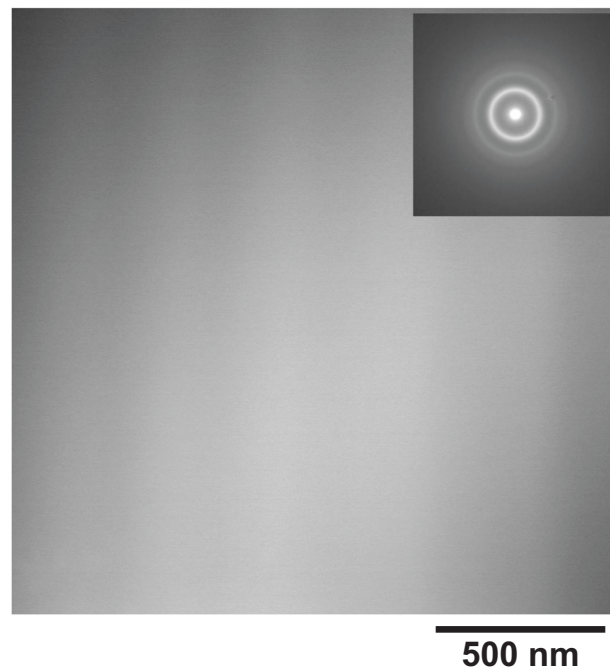


Fig. 4 Low-magnification BF-STEM images of the pHPQ $\text{Zr}_{50}\text{Cu}_{40}\text{Al}_{10}$ sample synthesized at 5.5 GPa and 880 K. Inset is the selected area diffraction pattern of the image. There is no contrast in the BF-STEM image and there are no spots corresponding to the crystal in the diffraction pattern, indicating no typical ordering at the 100-nm scale in the pHPQ sample. The vertical stripes are the processing trace by the focused ion beam.

pHPQ sample is a densely distributed nanocrystallized sample with the Cu-rich nanocrystals.

Effect of high-pressure annealing on mechanical properties.

We tested the mechanical properties of the $\text{Zr}_{50}\text{Cu}_{40}\text{Al}_{10}$ samples synthesized at high temperatures at 5.5 GPa. Figure 8 shows the effects of the high-pressure annealing at 5.5 GPa on the density, hardness, shear and bulk moduli, and compressive strength of the $\text{Zr}_{50}\text{Cu}_{40}\text{Al}_{10}$ BMG, along with results of ambient-pressure annealing. The densities of the HPQ and pHPQ samples are higher than those of the amorphous samples, and lower than those of the crystallized samples (Fig. 8a), which is consistent with the recent work¹⁶. The same trend is observed for the shear modulus (Fig. 8b).

The HPQ sample synthesized at 840 K and 5.5 GPa shows a marked densification (Fig. 8a); however, the Vickers hardness and bulk modulus do not show any significant change (Fig. 8c, d). In contrast, although the densities of the pHPQ samples are similar to that of the HPQ sample (Fig. 8a), the Vickers hardness and bulk modulus of the pHPQ sample synthesized at 880 K and 5.5 GPa exhibit significant increases of ~30% and 10%, respectively, compared to the as-cast values, which are even higher than those of the crystallized samples (Fig. 8c, d). In addition, the compressive strength and Young's modulus of the $\text{Zr}_{50}\text{Cu}_{40}\text{Al}_{10}$ BMG increase significantly for the pHPQ sample (Fig. 8e). The compressive strength and Young's modulus of the pHPQ sample synthesized at 880 K and 5.5 GPa are 2210 MPa and 126 GPa, respectively, while those of the as-cast sample are 1760 MPa and 95 GPa, respectively. The values of the pHPQ sample are also higher than those of the HPQ sample: 2074 MPa and 112.1 GPa, respectively¹⁶.

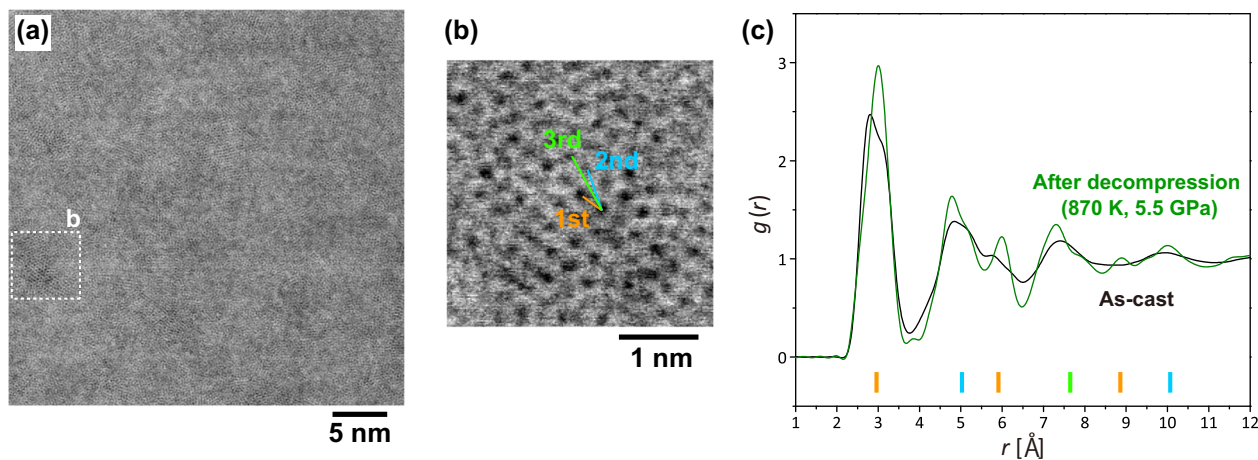


Fig. 5 High-magnification BF-STEM images of the pHQ $\text{Zr}_{50}\text{Cu}_{40}\text{Al}_{10}$ sample synthesized at 5.5 GPa and 880 K. **a** BF-STEM image of the sample. **b** High-magnification version of image in **a**. Atomic distances in the nano-ordered region are estimated to be the first (orange), second (light blue), and third (light green) neighbor distances of ~ 3.0 Å, ~ 5.0 Å, and ~ 7.6 Å, respectively. **c** Comparison between the atomic neighbor distances in **b** and $g(r)$. Black and green curves denote $g(r)$ of the as-cast sample, and the pHQ sample treated at 5.5 GPa and 870 K, respectively. Orange, light blue, and light green vertical bars denote the multiple values of the first, second, and third-neighbor distances, respectively.

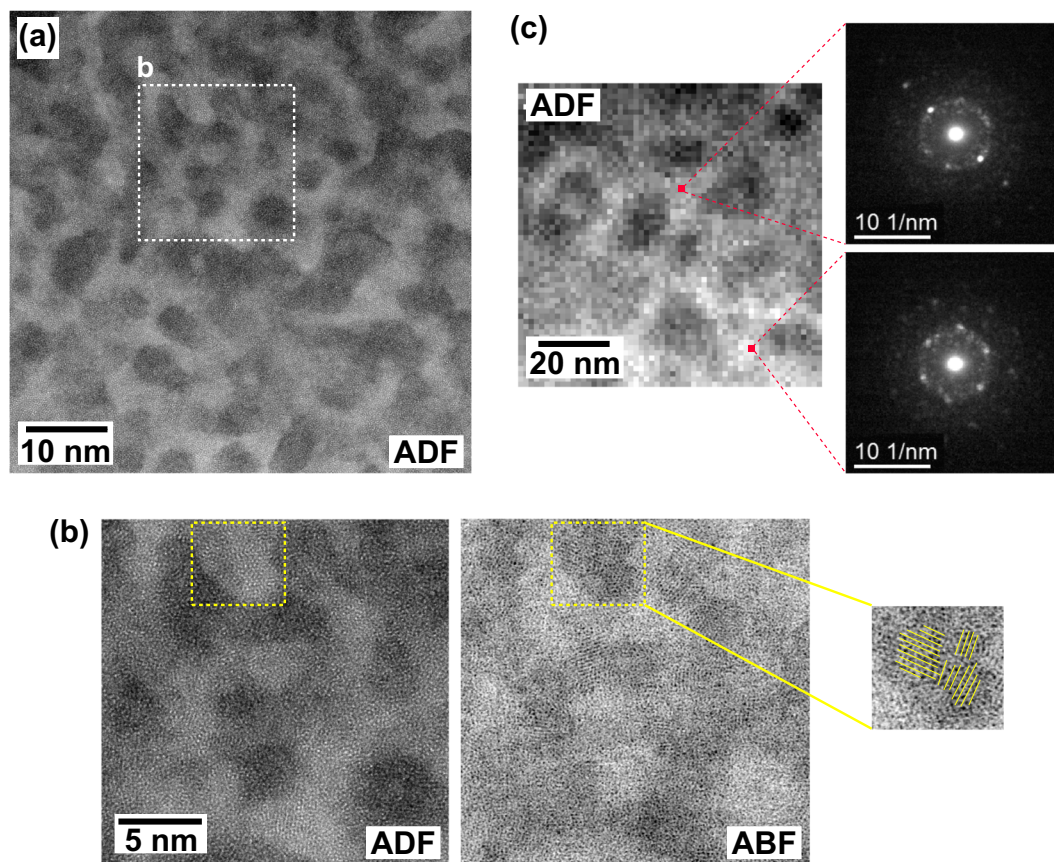


Fig. 6 ADF-STEM images of the pHQ $\text{Zr}_{50}\text{Cu}_{40}\text{Al}_{10}$ sample synthesized at 5.5 GPa and 880 K. **a** ADF-STEM image of the sample. **b** High-magnification version of image in **a**. Left and right images are the ADF-STEM, and ABF-STEM images, respectively. Yellow dotted square shows typical Cu-rich ordered region. Yellow lines are traces of fringe-like contrast in the yellow dotted square. **c** Nanobeam electron diffraction patterns in the bright area in the ADF-STEM image. Area is different from that of **a** in the same pHQ sample.

Discussion

Based on the EDS analyses, $\text{Cu}_{10}\text{Zr}_7$ (58.8 at.% Cu and 41.2 at.% Zr)¹⁸, Cu_2Zr Laves phase (66.7 at.% Cu and 33.3 at.% Zr)¹⁹, and AlCu_2Zr (25 at.% Al, 50 at.% Cu, and 25 at.% Zr)²⁰ may be good candidates for the Cu-rich nanocrystal (~ 33 at.% Zr, 59 at.% Cu, and 8 at.% Al) observed in this study in terms of composition,

although the exact crystal phase of the Cu-rich nanocrystal in this study is not clear. However, it is important to note that the primary phase of crystallization in Zr–Cu–Al MGs has been known to be a Zr-rich phase, such as Zr_2Cu , ZrCu , and the τ_3 phase^{20–23}, rather than Cu-rich phases. Furthermore, for achieving partial ordering and partial nanocrystallization in Zr–Cu–Al MGs at

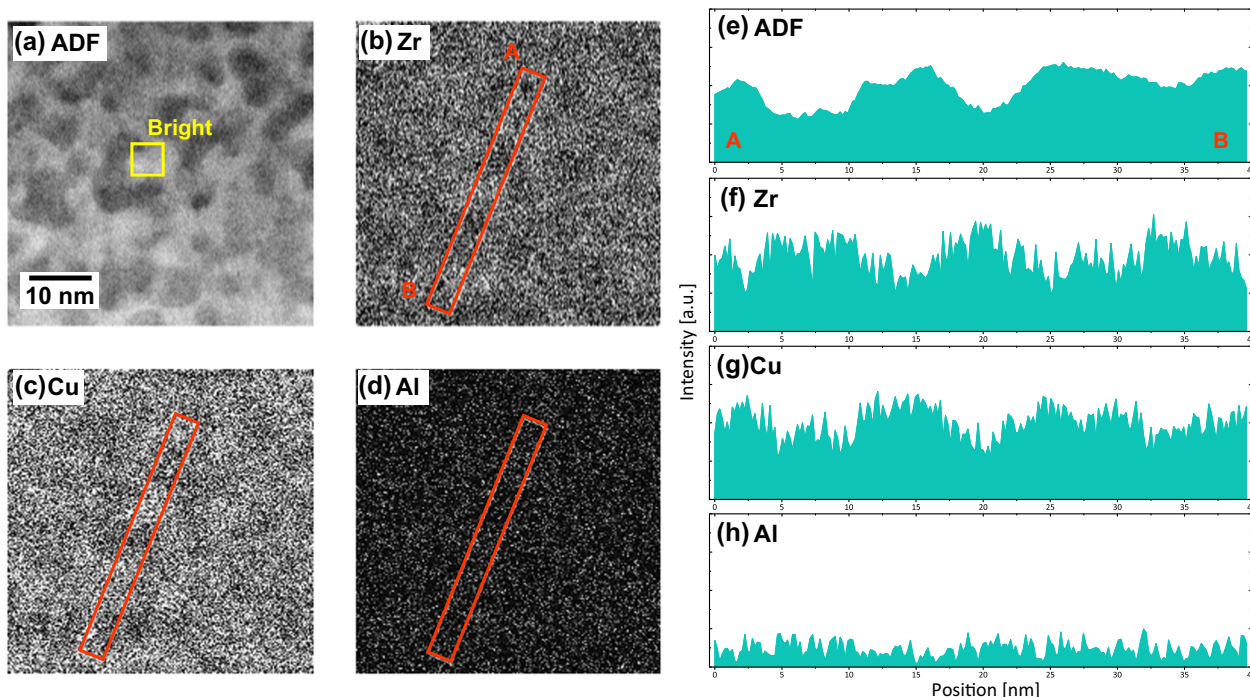


Fig. 7 EDS mapping analyses of the pHPQ sample. **a** ADF-STEM image of the pHPQ sample synthesized at 5.5 GPa and 880 K. Mapping of **b** Zr, **c** Cu, and **d** Al in the same area as **a**. Composition in yellow square in **a** is -33 at.% Zr, 59 at.% Cu, and 8 at.% Al in the bright area. Line profiles of **e** ADF, **f** Zr, **g** Cu, and **h** Al in the red A-B area.

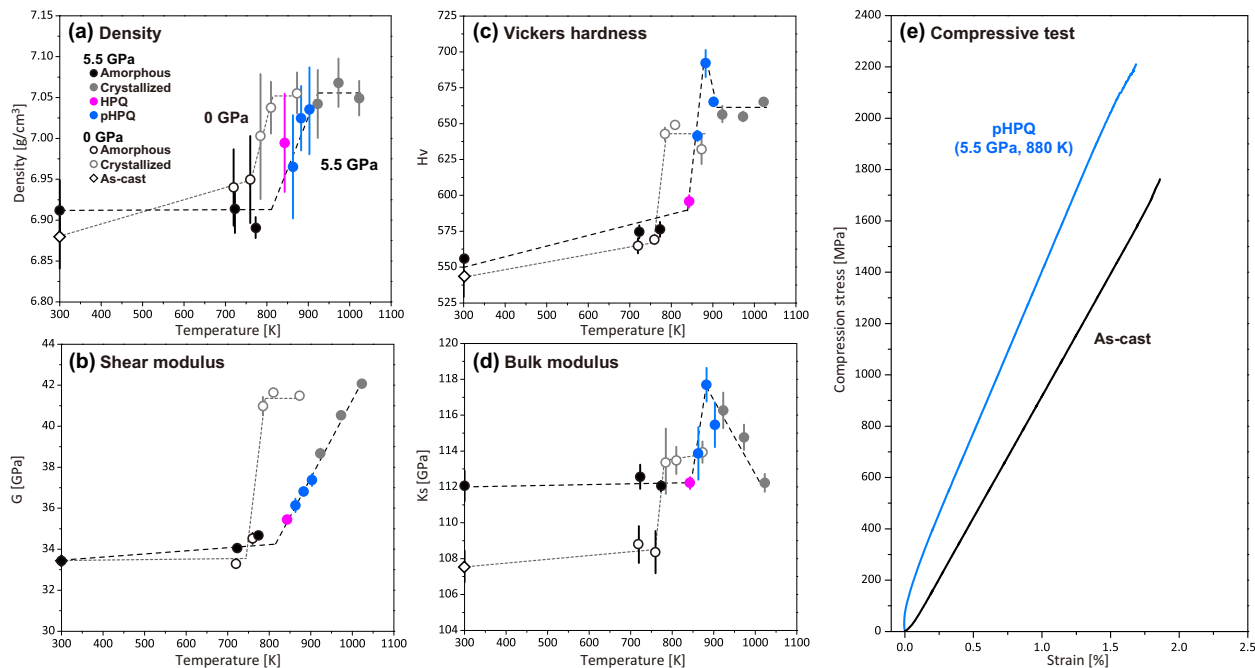


Fig. 8 Effect of high-pressure annealing on mechanical properties of the $Zr_{50}Cu_{40}Al_{10}$ BMG. **a** Density, **b** shear modulus, **c** Vickers hardness, and **d** bulk modulus as a function of synthesized temperature. Results of the ambient-pressure annealing are shown for comparison. Solid and open symbols denote the data at a synthesis pressure of 5.5 GPa and ambient pressure, respectively. Black and gray symbols denote the amorphous and crystallized samples, respectively. Purple and blue symbols denote the data of the HPQ and pHPQ samples, respectively. Open diamond denotes the data of the as-cast sample. Dashed and dotted lines are to guide the eyes. Errors are determined as two sigma of the standard deviation. The error bars fall within symbols if those do not appear. **e** Stress-strain curves of the as-cast (black) and pHPQ (blue) samples. The nonlinear behavior of the stress-strain curve of the pHPQ sample ~0% strain is probably due to the barreled shape of the sample after the high-pressure experiment. The compressive strength and Young's modulus of the pHPQ sample synthesized at 880 K and 5.5 GPa are 2210 MPa and 126 GPa, respectively, while those of the as-cast sample are 1760 MPa and 95 GPa, respectively.

ambient pressure, minor elements, such as Pd, Au, and Nb must be added to Zr–Cu–Al MGs to enhance the nucleation rate of crystals^{24–27} because the primary phase of Zr₂Cu or ZrCu has a small nucleation rate^{21,28}. Thus, the nucleation of Cu-rich crystals in the pHPQ sample as the primary phase and the formation of the densely distributed nanocrystallized texture without the addition of other elements do not agree with the understanding of crystallization in Zr–Cu–Al MGs at ambient pressure.

A previous study on high-pressure annealing⁶ showed that Zr₂Cu was crystallized as the first phase by annealing the Zr₅₅Al₁₀Ni₅Cu₃₀ BMG at 5 GPa, which is generally the same crystallization process as that at ambient pressure, but it is conflicting with our observations. The major difference between Zhang et al.⁶ and this study is the annealing temperature employed to obtain the crystallized sample. This study annealed the Zr₅₀Cu₄₀Al₁₀ BMG at 870–900 K, while the previous study⁶ annealed the Zr₅₅Al₁₀Ni₅Cu₃₀ BMG <800 K that may be below the temperature of the structural change at high pressures. We consider that the high-temperature annealing of the HPQ glass after the structural change may be a key to the unusual formation of the Cu-rich nanocrystals in the Zr₅₀Cu₄₀Al₁₀ BMG at high pressure and high temperature.

To investigate the change in atomic configurations at high pressure and high temperature more closely, we employed RMC modeling. The RMC modeling method has the advantage that a three-dimensional atomic configuration can be obtained using the experimental data. However, there is uncertainty in the atomic configuration of Al and Cu, when only the X-ray diffraction data set is used because the X-ray scattering intensities from these atoms are smaller than that from Zr. Therefore, we also conducted MD simulations to confirm the validity of a result of the RMC modeling. The RMC modeling was carried out by fitting to the $S(Q)$ data of the as-cast sample, and the samples before (700 K and 5.5 GPa) and after the structural change (850 K and 5.5 GPa). The RMC models well reproduced the experimentally obtained $S(Q)$ (Supplementary Fig. 1). The MD simulation also showed a similar structural change at high pressure and high temperature to the experimental results (Supplementary Fig. 2). The positions of the first maximum of partial pair distribution functions, $g_{ij}(r)$, in the as-cast sample, $r_{\text{Cu–Cu}} = 2.55$ Å, $r_{\text{Zr–Cu}} = 2.75$ Å, and $r_{\text{Zr–Zr}} = 3.15$ Å in the RMC modeling, and $r_{\text{Cu–Cu}} = 2.50$ Å, $r_{\text{Zr–Cu}} = 2.79$ Å, and $r_{\text{Zr–Zr}} = 3.18$ Å in the MD simulation, were generally in agreement with the data for Zr–Cu glasses reported by the previous studies^{17,29–32}. For both the RMC modeling and MD simulation, $g_{ij}(r)$ shows that the Zr–Zr distance decreases slightly after the change to the HPQ glass, whereas the Zr–Cu distance increases (Supplementary Fig. 3). The Cu–Cu distance is almost constant. These results indicate that the change of the first peak of $g(r)$ from the double-peak feature to the single-peak feature observed by X-ray diffraction experiments (Fig. 3) is caused by the distances becoming similar between Zr–Zr and Zr–Cu distances.

The RMC model of the HPQ glass exhibits fewer and smaller cavities compared to the glasses before the change to the HPQ glass (Supplementary Fig. 4), suggesting the dense packing structure of the HPQ glass. This is consistent with the density measurement (Fig. 8a). The average coordination numbers (CNs) around the Zr and Cu atoms in the Zr₅₀Cu₄₀Al₁₀ glass obtained by the RMC modeling and the MD simulation are shown in Supplementary Table 1. We discuss only the Zr-centered and Cu-centered CNs because Al is the minor element in the Zr₅₀Cu₄₀Al₁₀ glass. There are no significant changes in the total Zr-centered (CN_{Zr}) and Cu-centered (CN_{Cu}) CNs before and after the change to the HPQ glass. In contrast, partial CNs show small changes. The CNs of Zr around Zr (CN_{ZrZr}) and Cu around Cu (CN_{CuCu}) slightly decrease, while the CNs of Cu around

Zr (CN_{ZrCu}) and Zr around Cu (CN_{CuZr}) slightly increase via the change.

Based on the CNs obtained by the RMC modeling and MD simulation, the local chemical order can be quantified by the Cargill–Spaepen short-range order parameter³³ η , which is defined as:

$$\eta_{\text{AB}} = \text{CN}_{\text{AB}} / \text{CN}_{\text{AB}}^* - 1, \quad (1)$$

$$\eta_{\text{AA}} = -\eta_{\text{AB}}(x_{\text{B}}\text{CN}_{\text{B}}/x_{\text{A}}\text{CN}_{\text{A}}), \quad (2)$$

$$\eta_{\text{BB}} = -\eta_{\text{AB}}(x_{\text{A}}\text{CN}_{\text{A}}/x_{\text{B}}\text{CN}_{\text{B}}), \quad (3)$$

with $\text{CN}_{\text{AB}}^* = x_{\text{B}}\text{CN}_{\text{B}}\text{CN}_{\text{A}} / \langle \text{CN} \rangle$ and $\langle \text{CN} \rangle = x_{\text{A}}\text{CN}_{\text{A}} + x_{\text{B}}\text{CN}_{\text{B}} = x_{\text{A}}(\text{CN}_{\text{AA}} + \text{CN}_{\text{AB}}) + x_{\text{B}}(\text{CN}_{\text{BB}} + \text{CN}_{\text{BA}})$, where CN_{ij} is the CN of type j around type i and x_i is the fraction of type i in the sample. $\eta_{\text{AB}} = 0$ for complete chemical disorder, i.e., A and B atoms distribute randomly; $\eta_{\text{AB}} < 0$ for chemical preference against AB nearest-neighbor pairs, i.e., A and B atoms have a tendency to form clusters with each atom; $\eta_{\text{AB}} > 0$ for preferential chemical ordering between AB nearest-neighbor pairs, i.e., A and B atoms distribute more uniformly. As shown in Supplementary Table 1, in both cases of the RMC modeling and MD simulation, η_{ZrCu} is always positive, and it increases after the change to the HPQ glass. On the contrary, η_{ZrZr} and η_{CuCu} are negative. Although the absolute values of CN and η are different between the RMC modeling and MD simulation, two different methods show similar relative change at high pressure and temperature. These results indicate that the structure of Zr₅₀Cu₄₀Al₁₀ BMG changes to the dense packed structure and relatively chemical-uniform configuration after the change to the HPQ glass. It is generally considered that uniform mixing of large size Zr and small size Cu atoms easily achieves a dense packing structure. Thus, our results from the RMC modeling and MD simulations are consistent from the qualitative perspective. Such a preference for the Zr–Cu nearest-neighbor pairs at high pressure and high temperature may take place to achieve energy stabilization under high-pressure and high-temperature conditions, owing to the large negative mixing heat of -23 kJ mol⁻¹ between Zr and Cu³⁴.

Furthermore, we also observed intensity enhancements of atomic distances of ~ 3 , ~ 4.7 , and ~ 5.9 Å in $g(r)$ after the change to the HPQ glass (Fig. 9a). The enhancement of the atomic distance of ~ 3 Å, R_1 , which is at the first peak of $g(r)$, indicates that both Zr–Zr and Zr–Cu distances approach ~ 3 Å, and the short-range ordering with ~ 3 Å increases in the first coordination shell. In addition, the distances of ~ 5.9 and ~ 4.7 Å at the second peak of $g(r)$ are close to values of $2R_1$ (~ 6 Å) and $\sqrt{8/3}R_1$ (~ 4.9 Å), respectively. $2R_1$ and $\sqrt{8/3}R_1$ orderings are related to the connections between the first coordination shells (polyhedra) formed by atoms that are R_1 away from the central atom³⁵; $2R_1$ corresponds to the share of one atom between neighboring polyhedra, and $\sqrt{8/3}R_1$ corresponds to the share of three atoms. Enhancements of those positions suggest that the specific orderings (vertex and face sharing) are formed between neighboring first coordination polyhedra. The longer ordering with length of ~ 7.2 Å also appeared at the third peak of $g(r)$ (Fig. 9a).

Based on the above results, we propose the scenario of the structural change to the HPQ glass as follows. Zr and Cu (probably and Al) atoms are rearranged to form the dense packed structure by increasing the number of the nearest Zr–Cu pairs at high pressure and high temperature, resulting in the formation of the chemically uniform configuration. Simultaneously, each first coordination polyhedron also forms the specific orderings with neighboring polyhedra. Thus, the structural change to the HPQ glass is caused by formations of the medium-range ordering in the second- and third-neighbor distances, as well as the

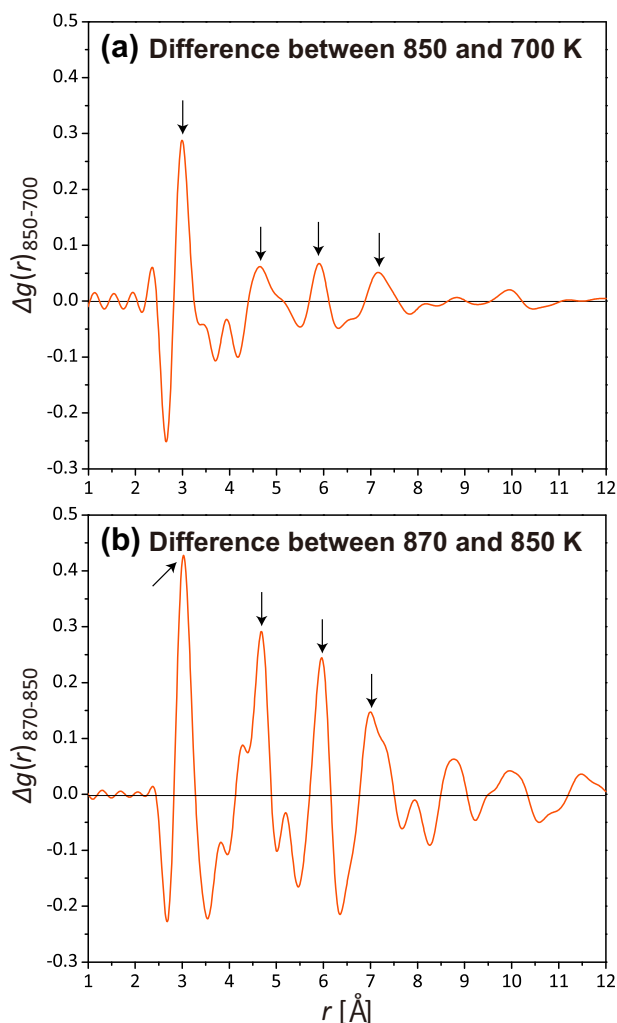


Fig. 9 Differences of experimentally obtained $g(r)$ between 850 and 700 K at 5.5 GPa and between 870 and 850 K at 5.5 GPa. **a** Difference of $g(r)$ before (700 K) and after (850 K, HPQ) the structural change at 5.5 GPa. **b** Difference of $g(r)$ between the samples treated at 870 K (pHPQ) and 850 K (HPQ) at 5.5 GPa. Arrows indicate enhanced distances at high temperatures at 5.5 GPa.

short-range ordering in the nearest-neighbor distance in the relatively chemically uniform configuration.

The enhanced distances after the change to the HPQ glass are close to those after the nanocrystallization (from HPQ to pHPQ; Fig. 9), which are also similar to the typical atomic neighbor distances in the nanocrystal observed in TEM image (Fig. 5). Therefore, the nanocrystal observed in the pHPQ sample may be formed based on the short-range and medium-range orderings formed by the structural change to the HPQ glass. In the chemically uniform configuration of the HPQ glass compared to that of the as-cast glass, Zr atoms should move more drastically than in the as-cast sample and long-range atomic diffusion is required, in order to form Zr-rich crystals, such as Zr_2Cu . However, the HPQ glass has the denser packing structure and the lower excess free volume than the as-cast glass, indicating that the atomic mobility and long-range diffusion are suppressed⁶. Because the large and heavy Zr atom would have a lower mobility than the small and light Cu atom in such dense packing structure, Zr-rich crystals are hard to crystallize. Although further investigations are required to understand the formation mechanism of Cu-rich

crystals at high pressure and high temperature, Cu atoms with high mobility may gather more easily than Zr atoms, resulting in the formation of Cu-rich crystal instead of Zr-rich crystal. Furthermore, the low atomic mobility under the high-pressure condition probably causes the crystal growth suppression. Therefore, the densely distributed Cu-rich nanocrystallized texture could be formed in the $\text{Zr}_{50}\text{Cu}_{40}\text{Al}_{10}$ BMG without the addition of other elements.

The partial nanocrystallization in BMGs has been reported to enhance mechanical properties by ambient-pressure studies^{24–27}. However, as shown in Fig. 10, the pHPQ sample in this study shows significant enhancements of the Vickers hardness, Young's modulus, and fracture strength of the $\text{Zr}_{50}\text{Cu}_{40}\text{Al}_{10}$ BMG compared to partially nanocrystallized glasses by compositional controls at ambient pressure. The values of the pHPQ $\text{Zr}_{50}\text{Cu}_{40}\text{Al}_{10}$ sample are considerably higher than the reported maximum values of nanocrystallized Zr-based BMGs, regardless of the similar volume fraction of nanocrystals. Such excellent mechanical properties of the pHPQ $\text{Zr}_{50}\text{Cu}_{40}\text{Al}_{10}$ sample may be caused by the small size of nanocrystals in the pHPQ sample. Inoue et al.²⁷ reported that the typical grain size in nanocrystallized Zr–Cu–Al–M(–Ni) ($M = \text{Pd}, \text{Au}, \text{Nb}, \text{Ag}, \text{or Pt}$) MGs is ~ 10 nm. In contrast, the grain size of the Cu-rich nanocrystals in the pHPQ $\text{Zr}_{50}\text{Cu}_{40}\text{Al}_{10}$ sample is estimated to be at least < 5 nm (Fig. 6). Such a small nanocrystal grain size in the pHPQ $\text{Zr}_{50}\text{Cu}_{40}\text{Al}_{10}$ sample may also be caused by the low atomic mobility under the high-pressure conditions. Even though further investigations are required to identify the mechanisms of the excellent mechanical properties of the pHPQ sample, high-pressure annealing enables us to improve the mechanical properties of Zr–Cu–Al BMGs without adding other elements, which has never been achieved at ambient pressure.

In conclusion, we found the unusual formation of densely distributed nanocrystallized $\text{Zr}_{50}\text{Cu}_{40}\text{Al}_{10}$ BMG through annealing at a high pressure of 5.5 GPa. The Cu-rich nanocrystals were nucleated in the $\text{Zr}_{50}\text{Cu}_{40}\text{Al}_{10}$ BMG via the pressure- and temperature-induced structural change to the ultra-dense HPQ glass that has the relatively chemically uniform configuration, with high short-range and medium-range orderings. The mechanical properties tests revealed that the densely distributed nanocrystallization in the $\text{Zr}_{50}\text{Cu}_{40}\text{Al}_{10}$ BMG at high pressure and high temperature significantly enhances hardness and strength. In the present study, we synthesized the nanocrystallized $\text{Zr}_{50}\text{Cu}_{40}\text{Al}_{10}$ BMG with a high nanocrystal volume fraction of ~ 60 – 70% through annealing at 880 K for 2 min at 5.5 GPa. However, it would be possible to change the volume fraction and size of nanocrystals by varying the synthesis temperature, pressure, and duration. High-pressure annealing opens a window to establish new procedures to create anomalous nanocrystallization textures, leading to the improvement and control of the properties of BMGs without a change in composition.

Methods

Sample preparation. An alloy ingot with the nominal composition of $\text{Zr}_{50}\text{Cu}_{40}\text{Al}_{10}$ was prepared through arc melting in an argon atmosphere. The glassy $\text{Zr}_{50}\text{Cu}_{40}\text{Al}_{10}$ alloy with a diameter of 4 mm and a height of 100 mm was obtained via tilt casting. The thermal properties of the glassy alloy were examined using a differential scanning calorimetry (DSC) under a heating rate of 20 K min^{-1} (the T_g of 703 K and the T_x of 790 K).

The high-pressure and high-temperature syntheses for STEM observations (Figs. 4–7), and mechanical properties measurements (Fig. 8) were carried out using a 1500-ton belt-type high-pressure apparatus installed at National Institute for Materials Science (NIMS), Japan. First, the pressure was increased to 5.5 GPa, and then the temperature was increased to a target temperature at a heating rate of 20 K min^{-1} . The sample was heated at the target temperature for 2 min and then quenched. The cooling rate was $\sim 100 \text{ K s}^{-1}$. We used boron nitride (BN) as the capsule. The sample was 4 mm in diameter and 3 mm in height. Heat treatment at

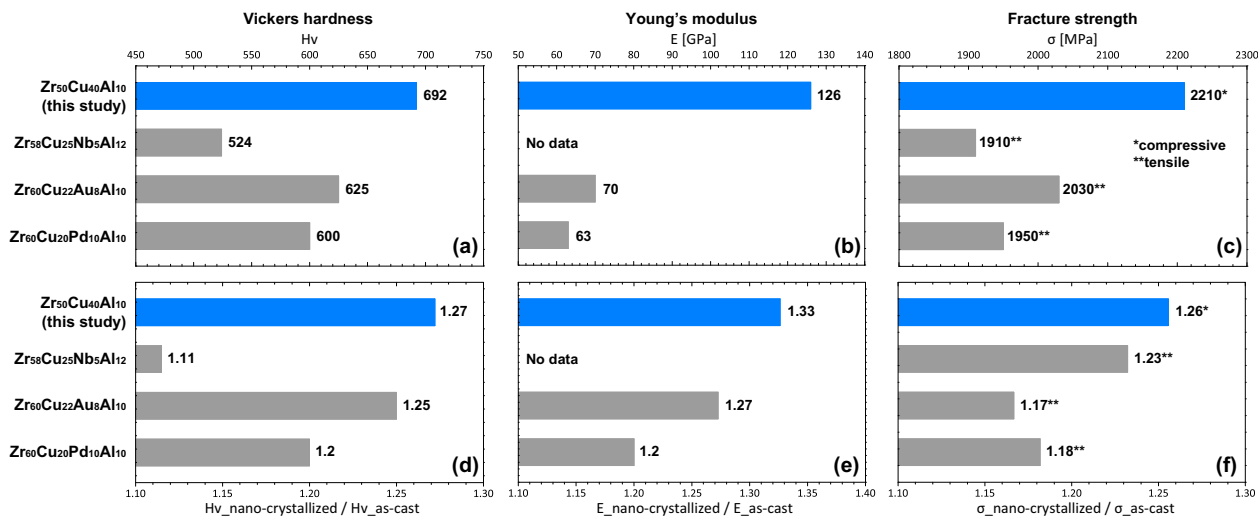


Fig. 10 Comparisons between the mechanical properties of nanocrystallized BMGs in the present study and previous ambient-pressure studies. **a** Vickers hardness (H_v), **b** Young's modulus (E), and **c** fracture strength (σ) of the pHQ Zr₅₀Cu₄₀Al₁₀ sample synthesized at 880 K and 5.5 GPa, Zr₆₀Cu₂₀Pd₁₀Al₁₀ with the volume fraction of nanocrystals (V_f) = 75% (ref. 27), Zr₆₀Cu₂₂Au₈Al₁₀ with V_f = 75% (ref. 27), and Zr₅₈Cu₂₅Nb₅Al₁₂ with V_f = 50% (ref. 26). Values of **d** H_v , **e** E , and **f** σ normalized by the values for the as-cast sample.

ambient pressure was performed using DSC at a heating rate of 20 K min⁻¹, a duration of 2 min, and a cooling rate of ~300 K min⁻¹.

The states of synthesized samples, i.e., amorphous, crystallized, or pHQ in Fig. 8, were identified by utilizing a Cu K_{α} X-ray diffractometer (Rigaku MiniFlex 600) installed at NIMS. A sample was classified as a crystallized sample if sharp X-ray diffraction peaks were observed and as a pHQ sample, if the intensities of the broad first and second peaks increased without sharp peaks (Supplementary Fig. 5). As the HPQ structure could not be identified by the Cu K_{α} X-ray diffractometer due to the minor change in XRD patterns, the HPQ sample in Fig. 8 was identified from the synthesis temperature conditions based on the synchrotron X-ray investigations (Fig. 1).

High-pressure structure measurement by synchrotron X-ray diffraction. High-pressure structure measurements were carried out using a Paris–Edinburgh (PE) large-volume press at beamline 16-BM-B, High Pressure Collaborative Access Team at the Advanced Photon Source³⁶. A pair of cup-shaped tungsten carbide anvils with cup diameters of 12 mm and bottom diameters of 3 mm were used to generate high pressures. The cell assembly used in this study is shown in Supplementary Fig. 6. The sample, with dimensions of ~0.5 × 0.5 × 0.3 mm, was placed at the center of the BN capsule. The thickness of the sample parallel to the X-ray was 0.3 mm. We used pyrolytic BN as the X-ray pass inside the BN capsule to minimize the diffraction peaks from the BN capsule in the XRD measurement. A MgO ring positioned adjacent to a graphite heater was used as the pressure standard with the equation of state of MgO³⁷. The EDXD patterns for MgO were collected for ~120 s at a fixed 2θ angle of 15° using a Ge solid-state detector (Ge-SSD; Canberra). Temperatures were estimated based on temperature–power relations at each load³⁶. The details of the high-pressure and high-temperature experiment performed using the PE press are provided in the previous study³⁶.

The structure measurements of the Zr₅₀Cu₄₀Al₁₀ BMG were conducted via the in situ multi-angle EDXD technique³⁶. The collimation system at the beamline 16-BM-B is established to control the collimation depth tightly³⁶, which is essential to minimize the background scattering from surrounding materials and obtain reliable structure data for the amorphous sample. We collected a series of EDXD patterns at 2θ angles of 4°, 5°, 7°, 9°, 12°, 16°, 22°, and 28° using the Ge-SSD. The slit sizes for the incident X-rays and the detector were adjusted at every 2θ angle to maximize the efficiency of data acquisition, while maintaining the Ge-SSD dead time at <15%. The total exposure time required to obtain a data set (eight EDXD patterns at different 2θ angles) was ~2 h. The primary structure factor result was derived from the observed EDXD patterns using a software package (aEDXD) developed by Dr. Park (see Kono et al.³⁶ for details). The observed EDXD patterns were normalized by assuming the effective background profile using the highest 2θ angle spectrum³⁶. The pair distribution function was obtained by the Fourier transform of the structure factor with a maximum Q (Q_{max}) of 15.0 Å⁻¹. We applied the Kaplow-type optimization procedure to determine the final structure factor, $S(Q)$, and pair distribution function, $g(r)$, using an optimization procedure described in Shen et al.³⁸.

First, we increased the pressure to 1.0 or 5.5 GPa, and then we increased the temperature to the target temperature. The sample was heated at the target temperature for 2 min, and then quenched to room temperature at high pressure. We collected the EDXD patterns of the sample under the high-pressure and room-temperature conditions. Then, we increased the temperature again to the next

target temperature at high pressure. We repeated this procedure up to the highest temperature.

STEM observations. The STEM observations were performed using a Titan³ G2 60–300 Probe Corrector (Thermo Fisher Scientific) operating at 300 kV installed at Tohoku University (Figs. 4 and 5), and the Titan³ (Thermo Fisher Scientific) operating at 300 kV installed at NIMS (Fig. 6a, b). The mapping experiment of the nanobeam electron diffraction (Fig. 6c) was performed by utilizing Titan³ at NIMS. Diffraction patterns were obtained for an area of 87 × 87 nm² at 1.5 nm intervals (3364 points). The probe profile of the mapping experiment of the nanobeam electron diffraction was limited by diffraction aberration because of the small convergence semi-angle (0.5 mrad). The probe size was estimated to be 2 nm in full-width at half-maximum. EDS analyses (Fig. 7) were performed by employing the Titan³ (20 kV) at NIMS. We estimated the volume fraction of nanocrystals from ADF-STEM image (Fig. 6a) using the image processing software “Image J” (<https://imagej.nih.gov/ij/>).

Density, hardness, and shear and bulk moduli measurements, and compression test. Density was measured based on Archimedes’ method using purified water. Vickers hardness was measured using a Vickers hardness tester (Matsuzawa MV-1S) at a load of 9.8 N with a dwell time of 10 s.

The elastic moduli of the samples were estimated from the sound velocities of the samples obtained by employing the pulse-echo overlap technique³⁹ using a waveform generator (Tektronix AWG2041) and a digital oscilloscope (Hewlett Packard 54522 A) installed at NIMS. The samples were mirrored on both surfaces. Longitudinal (L) and shear (T) wave signals were generated and received by a 10° Y-cut LiNbO₃ transducer with a thickness of 0.1 mm. An electrical sine wave was formed by the waveform generator, and ultrasonic echoes were observed using the digital oscilloscope. Frequencies of 37 and 20 MHz were used for L and T waves, respectively. The longitudinal velocity, V_L , and transversal velocity, V_T , were obtained by dividing the sample thickness by the travel times of the L and T waves, respectively, where the sample thickness was measured by a micrometer. The shear modulus, G , and bulk modulus, K , were calculated using the equations $G = \rho V_T^2$ and $K = \rho[V_L^2 - (4/3)V_T^2]$, respectively, where ρ is the density obtained using Archimedes’ method.

Compression tests were performed using the INSTRON 5982 compression tester installed at Tohoku University. Plastic strain was calculated from the strain at the deviation point of the linear region in the stress–strain curve to that at the final fracture. Young’s modulus was estimated from the linear region in the stress–strain curve.

Reverse Monte Carlo modeling. The standard RMC algorithm⁴⁰ was used for fitting the synchrotron X-ray diffraction data. The RMC models were constructed in cubes with periodic boundary conditions starting from random atomic configurations. The total number of atoms was 10,000, i.e., Zr: 5000, Cu: 4000, and Al: 1000. The density of the as-cast sample was calculated from the measured bulk density, while the densities for the synchrotron X-ray diffraction data obtained under 5.5 GPa were estimated from the first peak position of $S(Q)$, Q_1 , assuming $V \sim 1/Q_1^{2.5}$ reported by Zeng et al.⁴¹. The closest allowed distances for Zr–Zr, Zr–Cu, Zr–Al, Cu–Cu, Cu–Al, and Al–Al pairs were set to be 2.5, 2.3, 2.4, 2.1, 2.2,

and 2.3 Å, respectively, based on a previous study¹⁷. The r -spacing of the partial pair distribution functions $g_{ij}(r)$ was set to be 0.1 Å. The cut off distances, $r_{\text{cut off}}$ for calculating CNs were determined from the maximum ranges of the first shell distribution in each $g_{ij}(r)$.

Molecular dynamics analysis of the effects of a thermal process and hydrostatic pressure on the internal structure. Using a MD framework, we constructed $\text{Zr}_{50}\text{Cu}_{40}\text{Al}_{10}$ models by the melt-quenching process and the subsequent thermal loading process under hydrostatic pressure. The number of atoms in each model was 50,000. We used interatomic potentials developed for $\text{Zr}_{50}\text{Cu}_{40}\text{Al}_{10}$ alloys⁴². First, we constructed an as-cast model by quenching from 2000 to 300 K with a constant cooling rate of 10^{12} K s^{-1} under a constant pressure of 0 GPa. Subsequently, the thermal loading process under hydrostatic pressure was applied to the as-cast model as follows¹⁵. After a compressive 5.5 GPa pressure was applied to the as-cast model at 300 K, the model was heated to 850 K at a constant heating rate of 10^{13} K s^{-1} under a pressure of 5.5 GPa. Next, the model was relaxed at 850 K for 5 ns and cooled again to 300 K at a constant cooling rate of 10^{12} K s^{-1} under the 5.5 GPa pressure condition. Finally, the pressure was reduced to 0 GPa at 300 K. The model shape was altered so as to adjust the pressure condition during the entire thermal loading process. The r -spacing of partial pair distribution functions $g_{ij}(r)$ was set to 0.01 Å.

Data availability

The data that support the findings of this study are available from the corresponding author upon reasonable request.

Received: 10 September 2019; Accepted: 1 July 2020;

Published online: 07 August 2020

References

- Asami, K., Kawashima, A. & Hashimoto, K. Chemical properties and applications of some amorphous alloys. *Mater. Sci. Eng.* **99**, 475–481 (1988).
- Masumoto, T. & Maddin, R. The mechanical properties of palladium 20 at% silicon alloy quenched from the liquid state. *Acta Metall.* **19**, 725–741 (1971).
- Ashby, M. F. & Greer, A. L. Metallic glasses as structural materials. *Scr. Mater.* **54**, 321–326 (2006).
- Duwez, P. & Lin, S. C. H. Amorphous ferromagnetic phase in iron-carbon-phosphorus alloys. *J. Appl. Phys.* **38**, 4096–4097 (1967).
- Wang, W. H., He, D. W., Zhao, D. Q., Yao, Y. S. & He, M. Nanocrystallization of ZrTiCuNiBeC bulk metallic glass under high pressure. *Appl. Phys. Lett.* **75**, 2770–2772 (1999).
- Zhang, J. et al. Crystallization kinetics and pressure effect on crystallization of $\text{Zr}_{55}\text{Al}_{10}\text{Ni}_5\text{Cu}_{30}$ bulk metallic glass. *Mater. Sci. Eng. A* **357**, 386–391 (2003).
- Jiang, J. Z., Roseker, W., Sikorski, M., Cao, Q. P. & Xu, F. Pressure effect of glass transition temperature in $\text{Zr}_{46.8}\text{Ti}_{8.2}\text{Cu}_{7.5}\text{Ni}_{10}\text{Be}_{27.5}$ bulk metallic glass. *Appl. Phys. Lett.* **84**, 1871–1873 (2004).
- Zeng, Q. et al. Pressure-induced elastic anomaly in a polyamorphous metallic glass. *Appl. Phys. Lett.* **110**, 221902 (2017).
- Sheng, H. W. et al. Polyamorphism in a metallic glass. *Nat. Mater.* **6**, 192–197 (2007).
- Zeng, Q. S. et al. Anomalous compression behavior in lanthanum/cerium-based metallic glass under high pressure. *Proc. Natl Acad. Sci. USA* **104**, 13565–13568 (2007).
- Zeng, Q. S. et al. Origin of pressure-induced polyamorphism in $\text{Ce}_{75}\text{Al}_{25}$ Metallic Glass. *Phys. Rev. Lett.* **104**, 105702 (2010).
- Liu, X. R. & Hong, S. M. Evidence for a pressure-induced phase transition of amorphous to amorphous in two lanthanide-based bulk metallic glasses. *Appl. Phys. Lett.* **90**, 251903 (2007).
- Li, G., Wang, Y. Y., Liaw, P. K., Li, Y. C. & Liu, R. P. Electronic structure inheritance and pressure-induced polyamorphism in lanthanide-based metallic glasses. *Phys. Rev. Lett.* **109**, 125501 (2012).
- Dmowski, W. et al. Pressure induced liquid-to-liquid transition in Zr-based supercooled melts and pressure quenched. *Sci. Rep.* **7**, 6564 (2017).
- Miyazaki, N., Wakeda, M., Wang, Y. J. & Ogata, S. Prediction of pressure-promoted thermal rejuvenation in metallic glasses. *npj Comput. Mater.* **2**, 16013 (2016).
- Yamada, R., Shibasaki, Y., Abe, Y., Ryu, W. & Saida, J. Unveiling a new type of ultradense anomalous metallic glass with improved strength and ductility through a high-pressure heat treatment. *NPG Asia Mater.* **11**, 72 (2019).
- Mattern, N. et al. Short-range order of Cu-Zr metallic glasses. *J. Alloys Compd.* **485**, 163–169 (2009).
- Takeuchi, A., Yubuta, K., Makino, A. & Inoue, A. Evaluation of glass-forming ability of binary metallic glasses with liquidus temperature, crystallographic

- data from binary phase diagrams and molecular dynamics simulations. *J. Alloy. Compd.* **483**, 102–106 (2009).
- Ryltsev, R. E., Klumov, B. A., Chitchev, N. M. & Shunyaev, K. Y. Nucleation instability in supercooled Cu-Zr-Al glass-forming liquids. *J. Chem. Phys.* **149**, 164502 (2018).
- Yamamoto, T. et al. Precipitation of the ZrCu B2 phase in $\text{Zr}_{50}\text{Cu}_{50-x}\text{Al}_x$ ($x=0, 4, 6$) metallic glasses by rapidly heating and cooling. *J. Mater. Res.* **25**, 793–800 (2010).
- Inoue, A., Kawase, D., Tsai, A. P., Zhang, T. & Masumoto, T. Stability and transformation to crystalline phases of amorphous Zr-Al-Cu alloys with significant supercooled liquid region. *Mater. Sci. Eng. A* **178**, 255–263 (1994).
- Yano, T. et al. Relaxation and crystallization behavior of the $\text{Zr}_{50}\text{Cu}_{40}\text{Al}_{10}$ metallic glass. *Mater. Trans.* **46**, 2886–2892 (2005).
- Yokoyama, Y. et al. Evolution of mechanical properties of cast $\text{Zr}_{50}\text{Cu}_{40}\text{Al}_{10}$ glassy alloys by structural relaxation. *Mater. Trans.* **46**, 2755–2761 (2005).
- Fan, C. & Inoue, A. Improvement of mechanical properties by precipitation of nanoscale compound particles in Zr-Cu-Pd-Al amorphous alloys. *Mater. Trans. JIM* **38**, 1040–1046 (1997).
- Fan, C., Takeuchi, A. & Inoue, A. Preparation and mechanical properties of Zr-based bulk nanocrystalline alloys containing compound and amorphous phases. *Mater. Trans. JIM* **40**, 42–51 (1999).
- Fan, C., Li, C. & Inoue, A. Nanocrystal composites in Zr-Nb-Cu-Al metallic glasses. *J. Non-Cryst. Solids* **270**, 28–33 (2000).
- Inoue, A., Fan, C., Saida, J. & Zhang, T. High-strength Zr-based bulk amorphous alloys containing nanocrystalline and nanoquasicrystalline particles. *Sci. Tech. Adv. Mater.* **1**, 73–86 (2000).
- Köster, U., Meinhardt, J., Roos, S. & Liebertz, H. Formation of quasicrystals in bulk glass forming Zr-Cu-Ni-Al alloys. *Appl. Phys. Lett.* **69**, 179–181 (1996).
- Chen, H. S. & Waseda, Y. Structure of glassy Zr-Cu and Nb-Ni alloys. *Phys. Stat. Sol.* **51**, 593–599 (1979).
- Mattern, N. et al. Phase separation and crystallization in Cu-Zr metallic glasses. *Mater. Trans.* **48**, 1639–1643 (2007).
- Park, E. S., Chang, H. J. & Kim, D. H. Effect of addition of Be on glass-forming ability, plasticity and structural change in Cu-Zr bulk metallic glasses. *Acta Mater.* **56**, 3120–3131 (2008).
- Kaban, I. et al. Local atomic arrangements and their topology in Ni-Zr and Cu-Zr glassy and crystalline alloys. *Acta Mater.* **61**, 2509–2520 (2013).
- Cargill, G. S. & Spaepen, F. Description of chemical ordering in amorphous alloys. *J. Non-Cryst. Solids* **43**, 91–97 (1981).
- Takeuchi, A. & Inoue, A. Classification of bulk metallic glasses by atomic size difference, heat of mixing and period of constituent elements and its application to characterization of the main alloying element. *Mater. Trans.* **46**, 2817–2829 (2005).
- Ding, J., Ma, E., Asta, M. & Ritchie, R. O. Second-nearest-neighbor correlations from connection of atomic packing motifs in metallic glasses and liquids. *Sci. Rep.* **5**, 17429 (2015).
- Kono, Y., Park, C., Kenney-Benson, C., Shen, G. & Wang, Y. Toward comprehensive studies of liquids at high pressures and high temperatures: combined structure, elastic wave velocity, and viscosity measurements in the Paris-Edinburgh cell. *Phys. Earth Planet. Inter.* **228**, 269–280 (2014).
- Kono, Y., Irifune, T., Higo, Y., Inoue, T. & Barnhoorn, A. P.-V-T relation of MgO derived by simultaneous elastic wave velocity and in situ X-ray measurements: a new pressure scale for the mantle transition region. *Phys. Earth Planet. Inter.* **183**, 196–211 (2010).
- Shen, G., Prakapenka, V. B., Rivers, M. L. & Sutton, S. R. Structural investigation of amorphous materials at high pressures using the diamond anvil cell. *Rev. Sci. Instrum.* **74**, 3021–3026 (2003).
- Higo, Y., Kono, Y., Inoue, T., Irifune, T. & Funakoshi, K. A system for measuring elastic wave velocity under high pressure and high temperature using a combination of ultrasonic measurement and the multi-anvil apparatus at SPring-8. *J. Synchrotron Rad.* **16**, 762–768 (2009).
- McGreevy, R. L. & Pusztai, L. Reverse Monte Carlo simulation: a new technique for the determination of disordered structures. *J. Mol. Simul.* **1**, 359–367 (1988).
- Zeng, Q. S. et al. General 2.5 power law of metallic glasses. *Proc. Natl Acad. Sci. USA* **113**, 1714–1718 (2016).
- Cheng, Y. Q., Ma, E. & Sheng, H. W. Atomic level structure in multicomponent bulk metallic glass. *Phys. Rev. Lett.* **102**, 245501 (2009).

Acknowledgements

The authors thank Dr. Taniguchi, Dr. Kohara, and Dr. Tsuchiya for useful discussions and suggestions. The authors also thank Curtis Kenney-Benson for technical support at Advanced Photon Source (APS). Y.S. acknowledges the support of JSPS KAKENHI Grant Number 15K17784 and 19K04992. J.S. acknowledges the support of JSPS KAKENHI Grant Number 18H03829. Y.K. acknowledges support by the National Science Foundation under Award No. EAR-1722495. Portions of this work were performed at HPCAT (Sector 16), APS, Argonne National Laboratory. HPCAT operations are

supported by Department of Energy (DOE)-NNSA's Office of Experimental Sciences. The Advanced Photon Source is a U.S. DOE Office of Science User Facility operated for the DOE Office of Science by Argonne National Laboratory under Contract No. DE-AC02-06CH11357. A part of this study was supported by Tohoku University Microstructural Characterization Platform in Nanotechnology Platform Project sponsored by the Ministry of Education, Culture, Sports, Science and Technology (MEXT), Japan. A part of this study was also supported by NIMS TEM Station.

Author contributions

Y.S., R.Y., J.S., Y.K., and M.W. designed the project. Y.S. wrote the paper with input from all authors. Y.S. and Y.K. performed in situ synchrotron X-ray experiments. Y.S. performed the high-pressure and high-temperature synthesis, and carried out the density, hardness, and elastic moduli measurements. R.Y. prepared the BMG, and performed the DSC experiments and compressive test. Y.S. analyzed the experimental data. M.N. and K.K. performed the TEM observations. K.I. and Y.S. conducted the RMC modeling. M.W. conducted the MD simulation. All authors discussed the results of the manuscript.

Competing interests

The authors declare no competing interests.

Additional information

Supplementary information is available for this paper at <https://doi.org/10.1038/s43246-020-00057-3>.

Correspondence and requests for materials should be addressed to Y.S.

Reprints and permission information is available at <http://www.nature.com/reprints>

Publisher's note Springer Nature remains neutral with regard to jurisdictional claims in published maps and institutional affiliations.



Open Access This article is licensed under a Creative Commons Attribution 4.0 International License, which permits use, sharing, adaptation, distribution and reproduction in any medium or format, as long as you give appropriate credit to the original author(s) and the source, provide a link to the Creative Commons license, and indicate if changes were made. The images or other third party material in this article are included in the article's Creative Commons license, unless indicated otherwise in a credit line to the material. If material is not included in the article's Creative Commons license and your intended use is not permitted by statutory regulation or exceeds the permitted use, you will need to obtain permission directly from the copyright holder. To view a copy of this license, visit <http://creativecommons.org/licenses/by/4.0/>.

© The Author(s) 2020